Strain-induced magnetic transitions in $SrMO_{2.5}$ (M = Mn, Fe) thin films with ordered-oxygen vacancies

Yongjin Shin and James M. Rondinelli*

Department of Materials Science and Engineering, Northwestern University, Evanston, Illinois 60208, USA

E-mail: jrondinelli@northwestern.edu

Abstract

We examine the epitaxial-strain-induced phase transitions in thin films of perovskite-derived $SrMnO_{2.5}$ and $SrFeO_{2.5}$ exhibiting ordered-oxygen vacancies (OOVs). We find that $SrMnO_{2.5}$ hosts multiple magnetic transitions to other ordered states, including antiferromagetic (AFM) and ferromagnetic (FM) orders of E*-AFM, C-AFM, and FM type depending on the compressive or tensile strain state. In contrast, no magnetic transitions occur in thin film $SrFeO_{2.5}$ (G-AFM to FM) whereas its bulk phase exhibits a hydrostatic pressure-induced antiferromagnetic-to-ferromagnetic transition. We explain the origin of these dependencies on the transition metal configuration, i.e., d^4 Mn versus d^5 Fe, and the relative orientation of the OOVs in the $Ca_2Mn_2O_5$-type structure type with respect to the epitaxial interface. We find that the magnetic phase stability can be predicted by using exchange striction arguments, with ferromagnetic (antiferromagnetic) spin interactions preferring longer (shorter) Mn-O bonds in the square pyramidal MnO_5 unit comprising $SrMnO_{2.5}$. Because the Mn-O bonds lengths directly shrink or elongate to accommodate the applied stress without considerable polyhedral rotations, we show that compressive and tensile strain tune the unit cell structure to favor different combinations of exchange interactions that stabilize the various magnetic spin orders. Our study shows that the strong coupling between the OOV structure and spin orders with epitaxial strain is a promising route to achieve picoscale control of functional electronic and magnetic responses in complex oxide thin films.

1 Introduction

The magnetic properties of transition metal oxides underscore many interesting fundamental phenomena, including colossal magnetoresistance (CMR),[1,2] which are promising mechanisms for next-generation memory devices.[3–5] The magnetic responses arise from competition among multiple magnetic states stabilized by small changes in the transition metal electronic configuration (filling), coordination environment, and polyhedral arrangement.[6–10] This sensitivity enables mechanical stimuli such as hydrostatic pressure, biaxial strain, and chemical pressure, to traverse magnetic phase boundaries.[11–14]

Ordered oxygen-vacancies (OOV) occur in derivative structures of ABO_3 perovskite, including brownmillerite, $Ca_2Mn_2O_5$-type, or $LaNiO_{2.5}$ structures.[7,15–17] They significantly impact magnetic properties in transition metal oxides[18] because they directly alter the transition-metal coordination and superexchange paths favoring different antiferromagnetic (AFM) or ferromagnetic (FM) interactions. For example, a zigzag E-type antiferromagnetic (E-AFM) order active in rare-earth perovskite manganites with MnO_6 octahedra,[14] can be readily stabilized in $SrMnO_{2.5}$ with the $Ca_2Mn_2O_5$-type structure[7] from MnO_5 illustrated in Fig. 1a by the structure-enabled nearest-neighbor Goodenough-Kanamori-Anderson (GKA) superexchange interactions.[19–21]

The ordered removal of oxygen ligands from the BO_6 octahedral units also reconstructs the coordination environment into square pyramidal, tetrahedral, and square planar geometries with varying crystal-field-splitting energies, changing the stability of high- and low-spin magnetic states tuned by external fields. Furthermore, the empty space at the vacancy site can accommodate stress induced changes to bond lengths and angles in ways unique from perovskite.[8] The anisotropic nature of OOVs produces inequivalent geometric orientations for thin film epitaxial strain.[22,23] For example, the (001) pseudocubic (pc) interface in the $Ca_2Mn_2O_5$-type structure can accommodate two different orientations as shown in Fig. 1c, which will affect superexchange interactions in different ways.

In this work, we report density functional theory (DFT) calculations of strained $SrMnO_{2.5}$

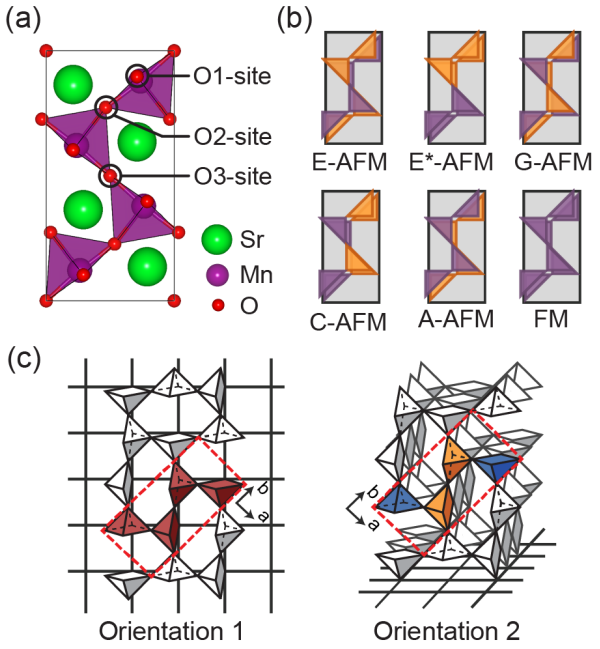

Figure 1: (a) Atomic structure of $SrMnO_{2.5}$ with three different oxygen sites: O1, O2, and O3. Schematic illustration of (b) possible magnetic orders in the $Ca_2Mn_2O_5$-type structure, and (c) available $(001)_{pc}$ interface orientations. The magnetic orders are indicated based on color: purple and orange polyhedra correspond to up-spin and down-spin polarized B cations, respectively.

and $SrFeO_{2.5}$ with the $Ca_2Mn_2O_5$-type OOV structure. $SrMnO_{2.5}$ exhibits the $Ca_2Mn_2O_5$-type structure in both single crystal and thin film form with a Néel temperature T_N of 375 K.[7,24] The $Ca_2Mn_2O_5$-type structure is also adopted by $SrFeO_{2.5}$ under high hydrostatic pressures (> 21 GPa),[25] while its magnetic response has not been experimentally verified. We find multiple magnetic transitions occur for biaxially strained $SrMnO_{2.5}$ under a $(001)_{pc}$ pseudocubic mechanical boundary condition. The equilibrium E-AFM order converts to an E*-AFM state follwed by a C-AFM state under compressive strain, while tensile strain drives transitions to E*-AFM and ultimately FM order. In contrast, $SrFeO_{2.5}$ maintains its G-AFM ground state order over the entire strain range explored. Comparing the magnetic stabilities with different biaxial orientations in $SrMnO_{2.5}$, we identify that the ratio of unit cell parameters and volume are predictive of the magnetic transitions due to compressive and tensile strain. As the magnetic orders prefer different picoscale distortions, manifesting as local changes in Mn-O bond lengths, we find mechanical stress leads to exchange striction

and allows for tuning among possible ordered spin states. We show these bond length changes are also correlated with changes in the lattice parameters in the different magnetic phase of $SrMnO_{2.5}$, making the latter effective proxies to predict the magnetic transitions.

2 Methods

We performed DFT calculations using the Vienna Ab-initio Simulations Package (VASP)[26,27] with the Perdew-Burke-Ernzerhof functional (PBE).[28] Projector-augmented wave (PAW) potentials[29] were used to describe the electron core-valence interactions with the following configurations: Sr ($4s^2 4p^6 5s^2$), Mn ($3d^6 4s^1$), Fe ($3d^7 4s^1$), and O ($2s^2 2p^4$). A high planewave cutoff of 850 eV is used to obtain the ground structures with a $8 \times 4 \times 6$ Monkhorst-Pack k-point mesh[30] for atomic relaxation and self-consistent total energy calculations of the $Ca_2Mn_2O_5$-type unit cells in Fig. 1a with multiple spin configurations (Fig. 1b). Brillouin zone integrations employed the tetrahedron method.[31] The cell volume and atomic positions were relaxed until the forces on each atom were less than $3\,\mathrm{meV\,\AA^{-1}}$

We account for electron-electron interactions using a static Coulomb interaction within the plus Hubbard U method of Dudarev *et al.*[32] The relative magnetic stabilities depend on the U value used, while their trends with respect to mechanical stress are independent of U as comprehensively discussed in a prior work.[8] Here we used $U(\mathrm{Mn}, d) = 3\,\mathrm{eV}$ and $U(\mathrm{Fe}, d) = 0\,\mathrm{eV}$ for the correlated d orbitals. These U values accurately capture the magnetic transitions as the energy difference between magnetic orders in $SrMnO_{2.5}$ decreases with U, wherase $U = 0\,\mathrm{eV}$ is preferred for $SrFeO_{2.5}$ because it stabilizes FM order with the spin-crossover transition. Thus these U values provide the lower bounds for mechanical strain driven magnetic transitions. The effects of U on the magnetic transitions at the critical strain values are discussed further in the Supporting Information (SI).

We simulated biaxial strain in Orientation 1 using a $1 \times 1 \times 2$ supercell consisting of 36 atoms and varying the length of the in-plane lattice constants given by $a{=}\sqrt{2}a_{pc}$ and

b=$2\sqrt{2}a_{pc}$, where a_{pc} is the pseudocubic lattice constant. We simulated the biaxial strain in Orientation 2 (Fig. 1c) using a supercell with lattice vectors ($2\vec{a}+\vec{b}$, $2\vec{c}$, $-2\vec{a}+\vec{b}$) such that the biaxial constraints are applied as ($4a_{pc}$, $2a_{pc}$, –). The k-point grid is scaled as necessary to obtain the same mesh density throughout. The two in-plane lattice parameters are then varied to mimic the biaxial constraints over a range of pseudocubic lattice constants spanning commercially available substrates.[33] Note that the two orientations yield different space groups for the $Ca_2Mn_2O_5$-type structure. While Orientation 1 does not lower the *Pbam* symmetry of bulk $SrMnO_{2.5}$, Orientation 2 reduces the symmetry to $P2/m$ as the applied biaxial constraints distort the orthorhombic lattice vectors.

We additionally note that the $Ca_2Mn_2O_5$-type structure is not the equilibrium phase of $SrFeO_{2.5}$; nonetheless, the structure is stabilized under high hydrostatic pressures, which agrees with the relatively small energy difference of ∼60 meV/f.u. between the $Ca_2Mn_2O_5$-type and equilibrium brownmillerite structures.[25] These aspects make $SrFeO_{2.5}$ an ideal system to compare with $SrMnO_{2.5}$ under epitaxial strain, although epitaxial $Ca_2Mn_2O_5$-type films of $SrFeO_{2.5}$ have not yet been realized experimentally.

3 Results and Discussion

Fig. 2 shows the relative magnetic stability of $SrMnO_{2.5}$ with respect to the pseudocubic lattice parameter a_{pc} describing the biaxial constraint. The lattice parameters of bulk orthorhombic $SrMnO_{2.5}$ (space group of *Pbam*) correspond to a_{pc} of 3.85 Å for the a axis and 3.95 Å for the b axis, respectively. Although Orientation 1 is more stable than Orientation 2 in general, we find Orientation 2 is more stable by up to 17 meV/f.u. for films with a_{pc} between 3.72 and 3.88 Å. First, unstrained $SrMnO_{2.5}$ subjected to the biaxial constraint favors E-AFM order. Next, we find that epitaxial strain drives a magnetic transition from E-AFM order to another spin order depending on the type of stress and the epitaxial orientation. With increasing tensile strain, we find that the E*-AFM then FM order become stable for both

orientations although the critical strain value for these transitions depends on the orientation. Upon increasing compressive strain, Orientation 1 exhibits magnetic transitions to E*-AFM and C-AFM while Orientation 2 maintains robustly the E-AFM order. This trend in the magnetic transitions persists independent of the value U, which is described in additional detail in the SI. Among the magnetic orders, only the metastable FM phase stabilized under compressive strain is metallic, denoted with filled symbols in Fig. 2, whereas the corresponding tensile-stabilized FM state is insulating (empty symbols). The metal-to-insulator transition with FM spin order is consistent with the expectation of changes in orbital overlap driven by strain. Increased overlap occurs under compressive strain, favoring metallicity, whereas the insulating phase arises under tensile strain as a consequence of the reduced orbital bandwidth and the square pyramidal crystal field splitting allowing integer electron filling supported by the finite Hubbard U value. All other magnetic transitions in $SrMnO_{2.5}$ occur without any metallization. Given that the local magnetic moments are weakly affect (varying over the range of 3.6-3.9 μ_B per atom), the high-spin configuration is also maintained (see SI).

To explain the magnetic transitions in $SrMnO_{2.5}$ under biaxial strain, we first identify the primary atomic structural changes that occur, focusing on Orientation 1. Fig. 3a shows the two primary changes with increasing tensile strain involve a monotonic increase in the unit cell volume while the c/a axial ratio decreases. These trends occur independent of the magnetic order, although we find minor variations for large compressive strains. The volume change can be understood intuitively as a linear response to the applied stress. The change in the c/a ratio reflects the anisotropy imposed by the strain state. The out-of-plane lattice constants increase relative to the in-plane lattice constants upon going from compressive to tensile strain in Orientation 1. Another structural change that occurs with biaxial strain is a variation in the metal–oxygen–metal bond angle, which we juxtapose in Fig. 4 with changes in stoichometric perovskites. As shown in Fig. 3b, the Mn-O-Mn angle on the O1-/O2-site decreases/increases with tensile strain. Here we note that the bond angle formed by the O3-site is always 180° owing to the site symmetry, and the bond angle formed by the

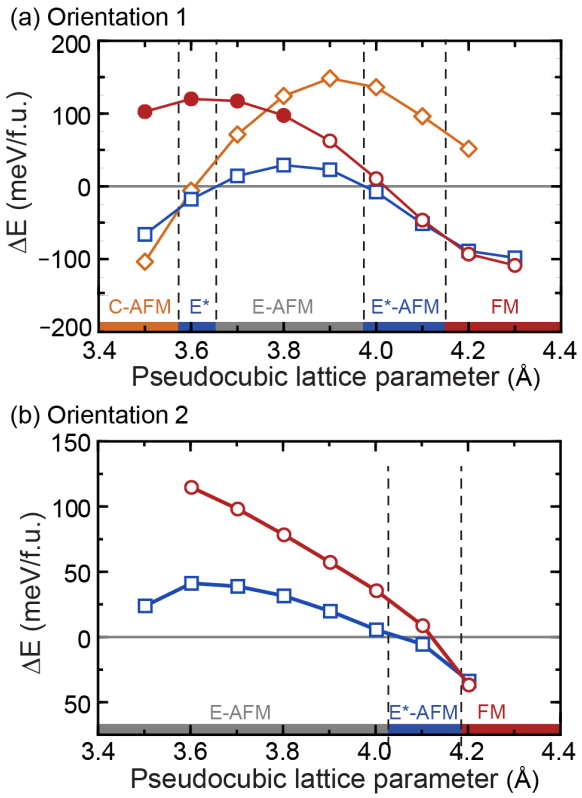

Figure 2: Relative energy difference for different magnetic orders in $SrMnO_{2.5}$ with biaxial strain for (a) Orientation 1 and (b) Orientation 2. Energies are compared to the AFM-E order in each pseudocubic lattice parameter value.

O2-site becomes larger than 180° and changes its bending direction at $a_{pc} = 4.3$ Å. These features agree with the cell parameter changes shown in Fig. 3a, where the bond angle evolves to better accommodate the "tetragonally" distorted unit cell, i.e., the Mn–O1–Mn angle becomes straighter to accommodate the elongated c-lattice parameter and the Mn–O2–Mn angle becomes more tilted obtuse to better utilize the empty space at the vacancy site by rotating the MnO_5 square pyramids. Indeed, we found that the Mn-Mn distance spanning across the vacancy site with E-AFM order is significantly reduced from 4.22 to 3.01 Å for a_{pc} ranging from 4.3 to 3.5 Å. This significant rotation of the MnO_5 square pyramids, without changing orientation with respect to the substrate, is an unique feature of the OOV structures compared to stoichiometric perovskites.[34–36]

Although the structural dependencies with strain are largely independent of the magnetic state, the unit cell structural features do affect the stability of the magnetic ground state in

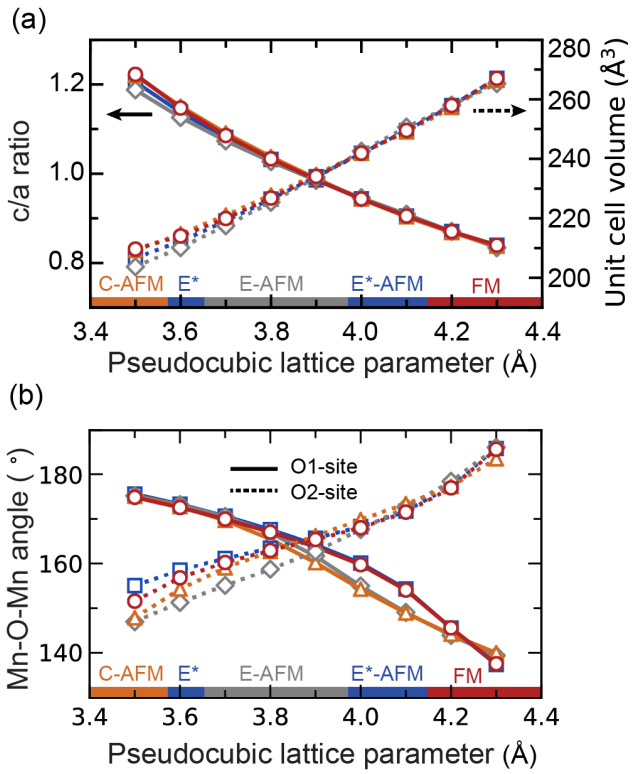

Figure 3: Variation in the (a) c/a-ratio (left ordinate) and unit cell volume (right ordinate), and (b) Mn-O-Mn bond angles of $SrMnO_{2.5}$ with respect to biaxial strain (Orientation 1) for different magnetic orders colored according to the magnetic state.

$SrMnO_{2.5}$ with biaxial strain, indicating an active magnetoelastic response due to exchange striction. To emphasize this coupling, we show in Fig. 5a the bulk lattice parameters and Mn-Mn distances without any structural constraints, and the corresponding bulk c/a ratio and unit cell volumes for different magnetic orders appear in Fig. 5b. The full crystallographic information for these phases are available in the SI. The FM state (stable at large tensile stresses) and the C-AFM state (stable at large compressive stresses) exhibit a large unit cell volume and a large c/a ratio, respectively. This can be understood on the grounds that FM spin order for d^4 Mn in a square pyramidal geometry weakens the $dp\sigma$ interactions. It is this hybridization that provides for superexchange among the basal-basal connection for the MnO_5 pyramids and leads to elongation of the Mn-O bond.[20] The superexchange asymmetry is amplified in the C-AFM state owing to chains of ferromagnetically aligned Mn, which prefer longer Mn-O bond lengths for the aforementioned reason relative to the shorter

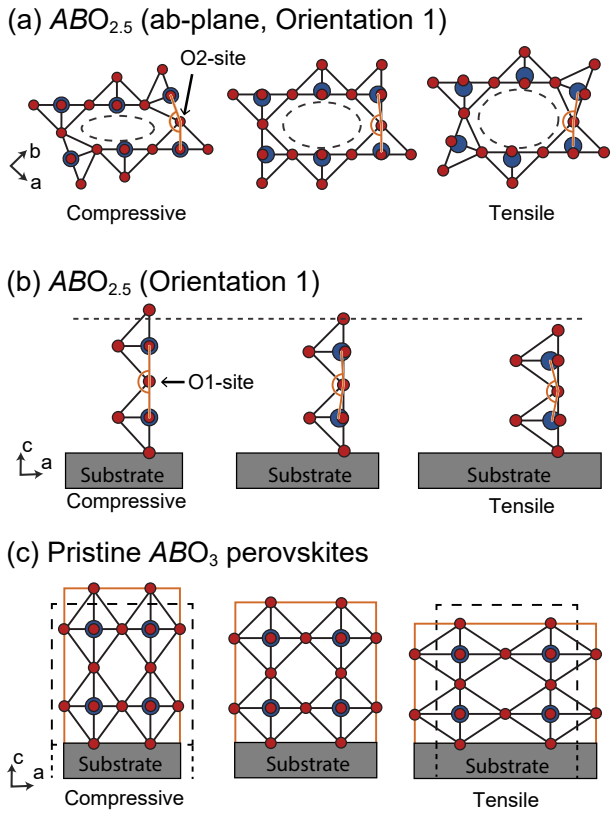

Figure 4: Schematic illustration of changes in the $Ca_2Mn_2O_5$-type structure with Orientation 1 under compressive/tensile strain: (a) *ab*-plane viewed from the *c* direction perpendicular to the substrate and (b) *ac*-plane viewed from the *b* direction. (c) Typical response of stoichiometric cubic perovskites to biaxial strain. Strain driven octahedral rotation and tilting effects, which often occur in perovskites, are not shown.

transverse Mn-O bonds that exhibit antiferromagnetic and stronger superexchange. Indeed, the in-plane and out-of-plane Mn-O bonds for the FM state are 1.99 Å and 1.95 Å, respectively. In contrast, the in-plane and out-of-plane Mn-O bonds for the C-AFM state are 1.96 Å and 1.96 Å, respectively. Although the magnitude of the bond lengths are different because of the strain state (compressive versus tensile), we find that the Mn-O-Mn interactions that are ferromagnetic (antiferromagnetic) are consistently longer (shorter). Thus, the biaxial strain applied with Orientation 1 allows $SrMnO_{2.5}$ to adopt local MnO_5 geometries favorable with the necessary exchange interactions that stablize different long-range ordered magnetic states.

We note that the $Ca_2Mn_2O_5$-type structure allows Mn-Mn pairs connected by the O3-site

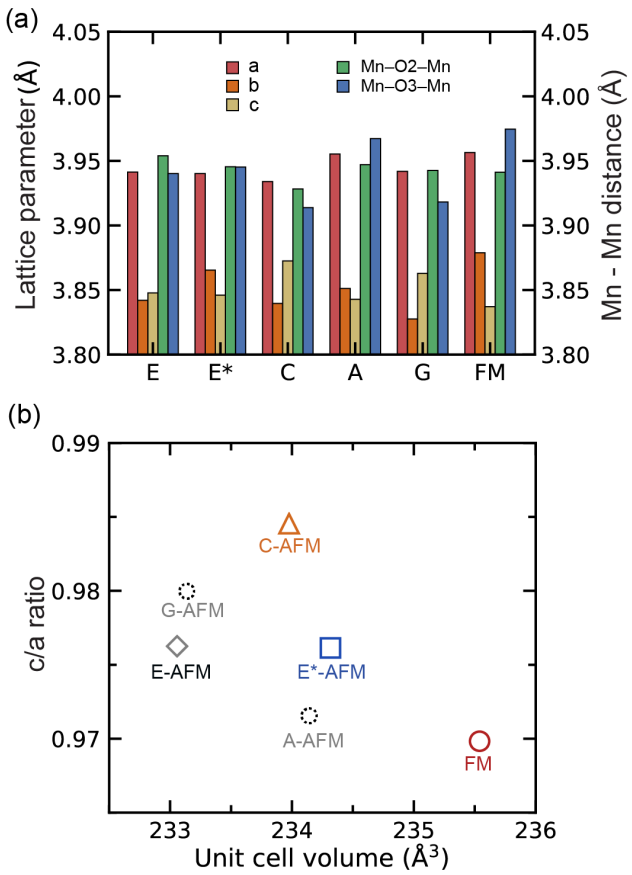

Figure 5: (a) The bulk (strain-free) lattice parameters and Mn-O-Mn distances over O2- and O3- bridging oxygen sites of different magnetic orders in *Pbam* $SrMnO_{2.5}$. (b) The bulk c/a ratio and unit cell volumes of different magnetic orders. The G-AFM and A-AFM orders do not appear in any of the strain-driven magnetic transitions and are denoted with dotted circles and gray text.

to also exhibit direct exchange across the vacancy site owing to the symmetric equivalence (see Fig. 1). In our previous work,[8] we identified that the Mn-Mn distance across the vacancy site is significantly reduced and the amplitude of direct exchange increases under hydrostatic pressure. We observe a similar reduction in this Mn-Mn distance under compressive biaxial strain with Orientation 1, and the magnetic coupling via direct exchange is correspondingly enhanced. The enhanced magnetic coupling further stabilizes the antiparallel spin alignment, increasing the energy penalty for ferromagntically aligned spins. Indeed, the FM state is unstable to other magnetic orders, such as E-, E*-, and C-AFM, whose magnetic coupling over vacancy site (and O3-site) is antiferromagnetic (Fig. 2a).

The exchange striction argument can be used to justify the stability of the other magnetic orders, although it becomes more complicated as the number of ferromagnetic and antiferromagnetic exchange-interactions changes for the different spin orders shown in Fig. 1b. For example, the A-AFM $SrMnO_{2.5}$ phase exhibits a larger unit cell volume but smaller axial ratio than the E-AFM order. The A-AFM and E-AFM spin orders are similar, however the A-AFM configuration has more ferromagnetic exchanges within the epitaxial plane for Orientation 1 than the E-AFM configuration, while unlike the E-AFM state, it has no antiferromagnetic exchange interactions in-plane. As a consequence, we expect the average in-plane bond lengths are longer for the A-AFM configuration than the E-AFM configuration, which leads to a larger a lattice constant for the A-AFM state than the E-AFM order. In the out-of-plane direction, the number of antiferromagnetic interactions is the same, suggesting similar out-of-plane Mn-O bond lengths and comparable c lattice parameters. Fig. 5a shows these Mn-O dependencies by comparing Mn-Mn distances over different oxygen sites. In particular, the Mn-Mn distance over O3-site is considerably longer for A-AFM, as A-AFM order imposes FM coupling unlike the ground state E-AFM order. As a result, the c/a ratio for the A-AFM state is smaller and its unit cell volume is larger than the E-AFM configuration.

The magnetoelastic response in $SrMnO_{2.5}$ at the bulk level provides an initial way to justify the stability of the magnetic states with strain. Fig. 3a shows the bulk E-AFM state transforms to an E*-AFM state under compressive strain in contrast to the bulk expectation that a magnetic phase with an axial ratio closer to unity (e.g., the G-AFM state) would be more likely preferred owing to a reduction (increase) in the a (c) lattice constants. However, the E*-AFM state is rather similar to C-AFM, which appears at large compressive strains, except the two configurations differ in the nature of the in-plane exchange interactions. In Orientation 1, the E*-AFM state has fewer antiferromagnetically coupled Mn spins, which leads to an a lattice parameter that will be larger than that preferred, i.e., energetically favored, by the C-AFM state for the same strain value. Indeed, the Mn-Mn distance over the

O2-site is 3.95 Å for E*-AFM, which is longer than 3.93 Å for the C-AFM order.

Interestingly, the E-AFM and E*-AFM states have nearly identical axial ratios, while the aformentioned argument is expected to lead to higher axial ratio for E*-AFM. Fig. 5a indicates that the a and c lattice parameters are nearly identical (less than 0.03% difference). We attribute this deviation from the exchange striction argument to the changes in bond angles, which compensate the longer bond length in $SrMnO_{2.5}$ with E*-AFM order. Indeed, the Mn-O bond lengths along the c axis of E- and E*-AFM are 1.94 and 1.95 Å, respectively, but the c lattice parameter is slightly smaller for E*-AFM. In addition, the largest difference in cell parameter is found for the b lattice parameter although the spin ordering on the ab-plane is the same for E- and E*-AFM orders. Thus the atomic structure dependencies with different magnetic orders occur with some secondary changes, permiting an exchange striction argument based on a structure map like Fig. 5b to be a useful guide for predicting magnetic stabilities.

The exchange striction model also applies to the magnetic order dependencies in Orientation 2, although the epitaxial relationship causes the in-plane and out-of-plane lattice constants of the film to be distinct from the simple crystallographic lattice parameters of the $Ca_2Mn_2O_5$-type structure. Similar to Orientation 1, tensile biaxial strain in Orientation 2 (Fig. 1c) increases the unit cell volume of $SrMnO_{2.5}$. The same magnetic transition sequence from E- to E*-AFM then to FM order occurs with tensile strain, although the critical strain values for the transitions slightly differ. In contrast, we did not find a magnetic transition with compressive strain since the lattice constant ratio favored by the C-AFM ordier is incompatible with the compressive strain and Orientation 2. With Orientation 2, the bulk c lattice vector aligns along the biaxial plane and corresponds to the in-plane lattice constants together while $2\vec{a}+\vec{b}$, and $-2\vec{a}+\vec{b}$ define the out-of-plane lattice constant. Thus the ratio of the out-of-plane to in-plane lattice constants is obtained as $|-2\vec{a}+\vec{b}|/|c|$ where a larger ratio occurs under compressive strain. The ratio of C-AFM is 1.004, smaller than the equilibrium E-AFM (1.011) state (see SI), which supports the absence of a magnetic transition under

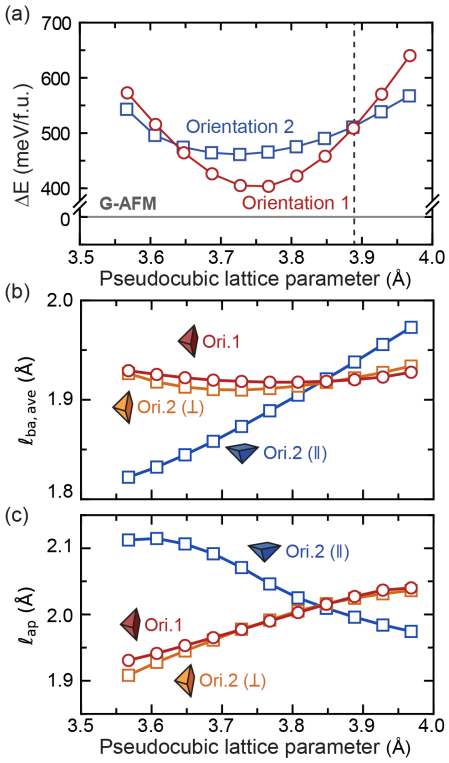

Figure 6: (a) Relative energy difference of FM $SrFeO_{2.5}$ phases compared to G-AFM phases with respect to biaxial strain in terms of pseudocubic lattice parameters with $U = 0$ eV. The dashed line of a_{pc} indicates the lattice parameters of bulk $SrFeO_{2.5}$ G-AFM phase. (b) Average basal bond length of the FeO_5 square pyramids ($\ell_{ba,ave}$), and (c) apical bond length (l_{ap}) for the unique square pyramidal units in the ferromagnetic phase of $SrFeO_{2.5}$ in Orientations 1 and 2. The geometry of the square pyramidal units with respect to biaxial plane follows Fig. 1c with $\perp$ and $||$ indicating the orientation of the pyramidal units with respect to the epitaxial plane.

compressive strain with Orientation 2.

Next, we examine whether similar magnetic transitions occur in strained $SrFeO_{2.5}$. Although a hydrostatic-pressure driven magnetic transition from G-AFM to FM order is predicted in $SrFeO_{2.5}$ at 21 GPa[8] in the $Ca_2Mn_2O_5$-type structure, we find that compressive biaxial strain does not stabilize a transition to the FM state (Fig. 6a). The minimum energy difference achieved by Orientation 1 and Orientation 2 are 400 meV/f.u. at 3.75 Å and 462 meV/f.u. at 3.72 Å, respectively. Consistent with the hydrostatic pressure report,[8] the FM phase of $SrFeO_{2.5}$ is metallic with strong $dp\sigma$ interactions. However, the FM metallic state achieved with hydrostatic pressure arises from a spin crossover. Unlike $SrMnO_{2.5}$, the

FM state in $SrFeO_{2.5}$ exhibits a unit cell volume that is smaller than its equilibrium G-AFM configuration. Indeed, the equilibrium pseudocubic lattice parameter of FM $SrFeO_{2.5}$, noted above, are well below the equilibrium lattice constant of the G-AFM phase, indicated with a dashed line in Fig. 6a. These lattice constants accessible with compressive strain are still greater than those required to drive the spin crossover, i.e., 3.52 Å for $U = 0$ eV, and thus the antiferromagnetic-to-ferromagnetic transition is absent.

Compressive strain is unable to access the required smaller unit cell volumes, and hence the shorter Fe-O bond lengths, needed to stabilize the FM order with low-spin state of Fe^{3+}. This limitation arises in part because the out-of-plane constant expands under compressive strain; for example, the in-plane lattice constants are compressed by ∼9.9% over the surveyed strain range, but at the same time the out-of-plane lattice constant elongates by ∼8.4%. Although the applied range of a_{pc} delivers comparable stresses as that obtained from hydrostatic pressures up to 30 GPa and above the critical value needed for the G-AFM to FM transition, the out-of-plane expansion effectively prevents the spin-crossover. The local FeO_5 units accommodate the applied stresses differently under the biaxial constraint as described next in detail for the FM spin order. Similar dependencies occur for the G-AFM phase (see SI).

The lattice constant dependencies are a consequence of the changes in the Fe-O bond network, which arises from the stress-induced changes to the corner-connected FeO_5 units. In Orientation 1, the basal plane of the FeO_5 unit is perpendicular to the epitaxial plane. As a result, upon going from compressive to tensile strain, we find that the basal Fe-O bonds, $\ell_{ba,ave}$, in the FM phase of $SrFeO_{2.5}$ exhibit weak dispersion (Fig. 6b). The apical Fe-O bond, ℓ_{ap}, is located within the epitaxial plane, and therefore it evolves nearly linearly with applied strain in Orientation 1. Orientation 2, in contrast, has two types of FeO_5 pyramids, which distort differently under biaxial compression: a pyramidal unit with its basal plane perpendicular to the biaxial plane (yellow) and a unit with its basal plane parallel to the biaxial plane (blue) as shown in panels (b) and (c) of Fig. 6. The yellow pyramid deforms from the applied stress in a manner similar to FeO_5 units active in Orientation 1, because the

units are oriented in the same geometry with respect to the strain boundary conditions. The Fe-O bond lengths in the blue pyramids, however, with the basal bonds within the epitaxial plane are strongly coupled to strain. All four bonds shorten under compressive strain, and therefore $\ell_{ba,ave}$ for Orientation 2 is smaller than that for Orientation 1. The response of the apical bond in this pyramid is anticorrelated with strain, and its length decreases upon going from compressive to tensile strain. These variations in bond lengths are distinct from those occurring under hydrostatic pressure,[8] where $\ell_{ba,ave}$ and ℓ_{ap} decrease simultaneously rather than bifurcating at large compressive strains.

4 Conclusion

We showed that the magnetic states in $Ca_2Mn_2O_5$-type structured oxides are tunable with biaxial strain owing to exchange striction. For d^4 $SrMnO_{2.5}$, strain led to magnetic transitions from E-AFM to E*-AFM, C-AFM, or FM order. In contrast for d^5 $SrFeO_{2.5}$, the pressure-dependent magnetic transition (G-AFM $\rightarrow$ FM) was inaccessible under compressive strain. The inaccessibility of the FM state is due to the anisotropic lattice deformations from biaxial strain with out-of-plane relaxations, which prohibits a spin crossover. We showed the magnetic stabilities under biaxial strain can be predicted via structural features. Understanding how OOV structures accommodate strain through changes in the metal-oxygen bond lengths and in the polyhedral rotation angles is essential. As the structural difference with magnetic orders are closely linked to the performance of magnetic applications,[37] our findings provide an effective strategy to control collectively ordered states in magnetic materials.

Acknowledgement

Y.S. and J.M.R. acknowledge support from the National Science Foundation (NSF) under award number DMR-2011208. Calculations were performed using the QUEST HPC Facility at Northwestern, the Extreme Science and Engineering Discovery Environment (XSEDE), which

is supported by the NSF under ACI-1548562, and the Center for Nanoscale Materials (Carbon) Cluster, an Office of Science user facility supported by the U.S. Department of Energy, Office of Science, Office of Basic Energy Sciences, under Contract No. DE-AC02-06CH11357.

Supporting Information Available

The Supporting Information is available free of charge on the ACS Publications website at DOI: Density of states of $SrFeO_{2.5}$ and the absence of spin transition with biaxial strain, crystallographic information of atomic structures of $SrMnO_{2.5}$ with varying magnetic order, magnetic moments of Mn and Fe in $SrMO_{2.5}$ (M = Mn, Fe), U-dependence of the magnetic transitions in $SrMnO_{2.5}$ (Orientation 1), characteristic bond lengths in $SrFeO_{2.5}$ with G-AFM magnetic order under biaxial strain, and a structure map of $SrMnO_{2.5}$ with Orientation 2.

References

(1) Ramirez, A. P. Colossal magnetoresistance. *Journal of Physics: Condensed Matter* **1997**, *9*, 8171–8199, DOI: 10.1088/0953-8984/9/39/005.

(2) Jin, S.; Tiefel, T. H.; McCormack, M.; Fastnacht, R. A.; Ramesh, R.; Chen, L. H. Thousandfold Change in Resistivity in Magnetoresistive La-Ca-Mn-O Films. *Science* **1994**, *264*, 413–415, DOI: 10.1126/science.264.5157.413.

(3) Pignard, S.; Vincent, H.; Sénateur, J. P.; Fröhlich, K.; Šouc, J. Effect of crystallinity on the magnetoresistive properties of $La_{0.8}MnO_{3-\delta}$ thin films grown by chemical vapor deposition. *Applied Physics Letters* **1998**, *73*, 999–1001, DOI: 10.1063/1.122065.

(4) von Helmolt, R.; Wecker, J.; Holzapfel, B.; Schultz, L.; Samwer, K. Giant negative magnetoresistance in perovskitelike $La_{2/3}Ba_{1/3}MnO_x$ ferromagnetic films. *Phys. Rev. Lett.* **1993**, *71*, 2331–2333, DOI: 10.1103/PhysRevLett.71.2331.

(5) Zhuang, W. W. et al. Novel colossal magnetoresistive thin film nonvolatile resistance random access memory (RRAM). Digest. International Electron Devices Meeting,. 2002; pp 193–196.

(6) Röder, H.; Zang, J.; Bishop, A. R. Lattice Effects in the Colossal-Magnetoresistance Manganites. *Phys. Rev. Lett.* **1996**, *76*, 1356–1359, DOI: 10.1103/PhysRevLett.76.1356.

(7) Caignaert, V.; Nguyen, N.; Hervieu, M.; Raveau, B. $Sr_2Mn_2O_5$, an oxygen-defect perovskite with Mn(III) in square pyramidal coordination. *Materials Research Bulletin* **1985**, *20*, 479 – 484, DOI: https://doi.org/10.1016/0025-5408(85)90101-1.

(8) Shin, Y.; Rondinelli, J. M. Pressure effects on magnetism in $Ca_2Mn_2O_5$-type ferrites and manganites. *Phys. Rev. B* **2020**, *102*, 104426, DOI: 10.1103/PhysRevB.102.104426.

(9) Millis, A. J.; Shraiman, B. I.; Mueller, R. Dynamic Jahn-Teller Effect and Colossal Magnetoresistance in $La_{1-x}Sr_xMnO_3$. *Phys. Rev. Lett.* **1996**, *77*, 175–178, DOI: 10.1103/PhysRevLett.77.175.

(10) Wollan, E. O.; Koehler, W. C. Neutron Diffraction Study of the Magnetic Properties of the Series of Perovskite-Type Compounds $[(1-x)\mathrm{La}, x\mathrm{Ca}]MnO_3$. *Phys. Rev.* **1955**, *100*, 545–563, DOI: 10.1103/PhysRev.100.545.

(11) González-Vázquez, O. E.; Íñiguez, J. Pressure-induced structural, electronic, and magnetic effects in $BiFeO_3$. *Phys. Rev. B* **2009**, *79*, 064102, DOI: 10.1103/PhysRevB.79.064102.

(12) Loa, I.; Adler, P.; Grzechnik, A.; Syassen, K.; Schwarz, U.; Hanfland, M.; Rozenberg, G. K.; Gorodetsky, P.; Pasternak, M. P. Pressure-Induced Quenching of the Jahn-Teller Distortion and Insulator-to-Metal Transition in $LaMnO_3$. *Physical Review Letters* **2001**, *87*, DOI: 10.1103/physrevlett.87.125501.

(13) Maurel, L.; Marcano, N.; Prokscha, T.; Langenberg, E.; Blasco, J.; Guzmán, R.; Suter, A.; Magén, C.; Morellón, L.; Ibarra, M. R.; Pardo, J. A.; Algarabel, P. A. Nature of antiferromagnetic order in epitaxially strained multiferroic $SrMnO_3$ thin films. *Physical Review B* **2015**, *92*, DOI: 10.1103/physrevb.92.024419.

(14) Picozzi, S.; Yamauchi, K.; Bihlmayer, G.; Blügel, S. First-principles stabilization of an unconventional collinear magnetic ordering in distorted manganites. *Phys. Rev. B* **2006**, *74*, 094402, DOI: 10.1103/PhysRevB.74.094402.

(15) Young, J.; Rondinelli, J. M. Crystal structure and electronic properties of bulk and thin film brownmillerite oxides. *Phys. Rev. B* **2015**, *92*, 174111, DOI: 10.1103/PhysRevB.92.174111.

(16) Sánchez, R. D.; Causa, M. T.; Caneiro, A.; Butera, A.; Vallet-Regí, M.; Sayagués, M. J.; González-Calbet, J.; García-Sanz, F.; Rivas, J. Metal-insulator transition in oxygen-deficient $LaNiO_{3-x}$ perovskites. *Phys. Rev. B* **1996**, *54*, 16574–16578, DOI: 10.1103/PhysRevB.54.16574.

(17) Anderson, M. T.; Vaughey, J. T.; Poeppelmeier, K. R. Structural similarities among oxygen-deficient perovskites. *Chemistry of Materials* **1993**, *5*, 151–165, DOI: 10.1021/cm00026a003.

(18) Walter, J.; Bose, S.; Cabero, M.; Varela, M.; Leighton, C. Giant anisotropic magnetoresistance in oxygen-vacancy-ordered epitaxial $La_{0.5}Sr_{0.5}CoO_{3-\delta}$ films. *Phys. Rev. Materials* **2020**, *4*, 091401, DOI: 10.1103/PhysRevMaterials.4.091401.

(19) Kanamori, J. Superexchange interaction and symmetry properties of electron orbitals. *Journal of Physics and Chemistry of Solids* **1959**, *10*, 87 – 98, DOI: https://doi.org/10.1016/0022-3697(59)90061-7.

(20) Goodenough, J. In Magnetism and the Chemical Bond; Cotton, FA; Olah, GA; Prigogine, I., Eds.; Interscience monographs Chemistry. 1963.

(21) Anderson, P. W. New Approach to the Theory of Superexchange Interactions. *Phys. Rev.* **1959**, *115*, 2–13, DOI: 10.1103/PhysRev.115.2.

(22) Inkinen, S.; Yao, L.; van Dijken, S. Reversible thermal strain control of oxygen vacancy ordering in an epitaxial $La_{0.5}Sr_{0.5}CoO_{3-\delta}$ film. *Phys. Rev. Materials* **2020**, *4*, 046002, DOI: 10.1103/PhysRevMaterials.4.046002.

(23) Inoue, S.; Kawai, M.; Ichikawa, N.; Kageyama, H.; Paulus, W.; Shimakawa, Y. Anisotropic oxygen diffusion at low temperature in perovskite-structure iron oxides. *Nature Chemistry* **2010**, *2*, 213–217, DOI: 10.1038/nchem.547.

(24) Wang, F.; Zhang, Y. Q.; Bai, Y.; Liu, W.; Zhang, H. R.; Wang, W. Y.; Li, S. K.; Ma, S.; Zhao, X. G.; Sun, J. R.; Wang, Z. H.; Wang, Z. J.; Zhang, Z. D. Oxygen vacancy formation, crystal structures, and magnetic properties of three $SrMnO_{3-\delta}$ films. *Applied Physics Letters* **2016**, *109*, DOI: 10.1063/1.4960463.

(25) Zhu, F.; Wu, Y.; Lai, X.; Qin, S.; Yang, K.; Liu, J.; Wu, X. Experimental and theoretical investigations on high-pressure phase transition of $Sr_2Fe_2O_5$. *Physics and Chemistry of Minerals* **2014**, *41*, 449–459, DOI: 10.1007/s00269-013-0604-6.

(26) Kresse, G.; Furthmüller, J. Efficient iterative schemes for *ab initio* total-energy calculations using a plane-wave basis set. *Phys. Rev. B* **1996**, *54*, 11169–11186, DOI: 10.1103/PhysRevB.54.11169.

(27) Kresse, G.; Joubert, D. From ultrasoft pseudopotentials to the projector augmented-wave method. *Phys. Rev. B* **1999**, *59*, 1758–1775, DOI: 10.1103/PhysRevB.59.1758.

(28) Perdew, J. P.; Burke, K.; Ernzerhof, M. Generalized Gradient Approximation Made Simple. *Phys. Rev. Lett.* **1996**, *77*, 3865–3868, DOI: 10.1103/PhysRevLett.77.3865.

(29) Blöchl, P. E. Projector augmented-wave method. *Phys. Rev. B* **1994**, *50*, 17953–17979, DOI: 10.1103/PhysRevB.50.17953.

(30) Monkhorst, H. J.; Pack, J. D. Special points for Brillouin-zone integrations. *Phys. Rev. B* **1976**, *13*, 5188–5192, DOI: 10.1103/PhysRevB.13.5188.

(31) Blöchl, P. E.; Jepsen, O.; Andersen, O. K. Improved tetrahedron method for Brillouin-zone integrations. *Phys. Rev. B* **1994**, *49*, 16223–16233, DOI: 10.1103/PhysRevB.49.16223.

(32) Dudarev, S. L.; Botton, G. A.; Savrasov, S. Y.; Humphreys, C. J.; Sutton, A. P. Electron-energy-loss spectra and the structural stability of nickel oxide: An LSDA+U study. *Phys. Rev. B* **1998**, *57*, 1505–1509, DOI: 10.1103/PhysRevB.57.1505.

(33) Schlom, D. G.; Chen, L.-Q.; Pan, X.; Schmehl, A.; Zurbuchen, M. A. A Thin Film Approach to Engineering Functionality into Oxides. *Journal of the American Ceramic Society* **2008**, *91*, 2429–2454, DOI: 10.1111/j.1551-2916.2008.02556.x.

(34) Rondinelli, J. M.; Coh, S. Large Isosymmetric Reorientation of Oxygen Octahedra Rotation Axes in Epitaxially Strained Perovskites. *Phys. Rev. Lett.* **2011**, *106*, 235502, DOI: 10.1103/PhysRevLett.106.235502.

(35) Moreau, M.; Marthinsen, A.; Selbach, S. M.; Tybell, T. First-principles study of the effect of (111) strain on octahedral rotations and structural phases of $LaAlO_3$. *Phys. Rev. B* **2017**, *95*, 064109, DOI: 10.1103/PhysRevB.95.064109.

(36) Lee, J. H.; Delaney, K. T.; Bousquet, E.; Spaldin, N. A.; Rabe, K. M. Strong coupling of Jahn-Teller distortion to oxygen-octahedron rotation and functional properties in epitaxially strained orthorhombic $LaMnO_3$. *Phys. Rev. B* **2013**, *88*, 174426, DOI: 10.1103/PhysRevB.88.174426.

(37) Bocarsly, J. D.; Levin, E. E.; Garcia, C. A. C.; Schwennicke, K.; Wilson, S. D.; Seshadri, R. A Simple Computational Proxy for Screening Magnetocaloric Compounds. *Chemistry of Materials* **2017**, *29*, 1613–1622, DOI: 10.1021/acs.chemmater.6b04729.

TOC Graphic

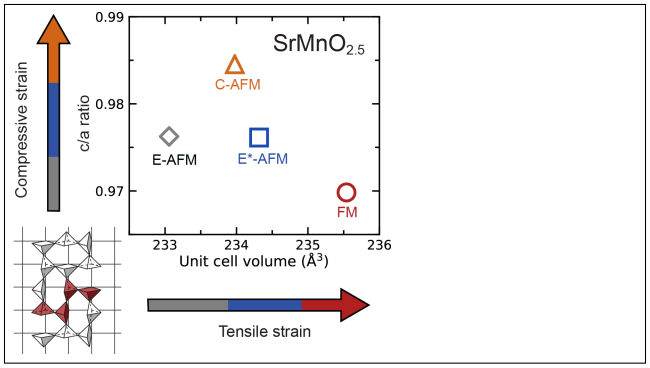

Magnetic structure map of $SrMnO_{2.5}$ in the space spanned by the c/a ratio and unit cell volume. These structural features are directly deformed by compressive and tensile strain, respectively, and are able to predict the corresponding magnetic transitions.